Regular Article

Exact partition potential for model systems of interacting electrons in 1-D[⋆]

Yan Oueis[1,a] and Adam Wasserman[1,2]

[1] Department of Chemistry, Purdue University, West Lafayette, IN 47907, USA
[2] Department of Physics and Astronomy, Purdue University, West Lafayette, IN 47907, USA

Abstract. We find the numerically exact partition potential for 1-D systems of interacting electrons designed to model diatomic molecules. At integer fragment occupations, the kinetic contribution to the partition potential develops sharp features in the internuclear region that nearly cancel corresponding features of exchange-correlation. They occur at locations that coincide with those of well-known features of the underlying molecular Kohn–Sham potential. For non-integer fragment occupations, we demonstrate that the fragment energy gaps determine the kinetic part of the partition potential. Our results highlight the importance of non-additive noninteracting kinetic and exchange-correlation energy approximations in density-embedding methods at large internuclear separations and the importance of non-additive noninteracting kinetic energy approximations at *all* separations.

1 Introduction

The modern approach to the theory of chemical change is deeply rooted in the formalism of density functional theory (DFT). The foundation was built by Parr, Yang, Ayers, Geerlings and others [1–4]. It is based on the analysis of the change to the ground state properties of isolated molecular fragments induced by other fragments approaching from infinity [5]. This approach made it possible to identify some of the most common pre-DFT reactivity indices with functional derivatives of the ground state molecular quantities. Nevertheless, the theory lacks the finite-distance interactions that play an essential role in the fragment chemical behavior. Noticeably, the formulation of Parr's reactivity indices within the non-integer DFT formalism (PPLB formalism) [6] leads to conceptually inconsistent results [5].

The partition theory (PT) of reference [5] aims at solving these inconsistencies. PT imagines a fictitious system of noninteracting fragments embedded in a global potential (*i.e.* same for all fragments). The fragments are constrained to have densities that sum to the total molecular density while minimizing the sum of fragment energies (more on this quantity later). The uniqueness of the fragment densities is ensured by the global embedding potential, according to the theorem of reference [7].

To formally introduce the PT, we partition the external potential $v(\mathbf{r})$ into fragments labeled by the index α:

$$v(\mathbf{r}) = \sum_\alpha v_\alpha(\mathbf{r}). \tag{1}$$

PT is based on the following decomposition of the molecular ground state (GS) energy:

$$E_v[n_{\mathrm{GS}}] = \min_{n_N \to N} \left[\min_{\{n_\alpha\} \to n_N} [E_{\mathrm{f}}[\{n_\alpha\}]] + E_{\mathrm{p}}[n_N] \right], \quad (2)$$

where $E_{\mathrm{f}}[\{n_\alpha\}]$ is the sum of fragment energies and $E_{\mathrm{p}}[n_N]$ is the partition energy. In equation (2), the outer minimization is over all densities that integrate to N electrons. Each of the fragment contributions to E_{f} is defined to have the PPLB functional form:

$$E_{\mathrm{f}}[\{n_\alpha\}] = \sum_\alpha \left\{ (1 - \omega_\alpha) E_{v_\alpha}[n_{p_\alpha}] + \omega_\alpha E_{v_\alpha}[n_{p_\alpha+1}] \right\}, \tag{3}$$

where p_α and ω_α are the integer and fractional parts of N_α (number of electrons in fragment α). The inner minimization in (2) is over all p_α, ω_α, $n_{p_\alpha}(\mathbf{r})$, and $n_{p_\alpha+1}(\mathbf{r})$ that produce the density $n_{\mathrm{f}}(\mathbf{r}) = n_N(\mathbf{r})$ according to:

$$n_{\mathrm{f}}(\mathbf{r}) = \sum_\alpha \left\{ (1 - \omega_\alpha) n_{p_\alpha}(\mathbf{r}) + \omega_\alpha n_{p_\alpha+1}(\mathbf{r}) \right\}. \tag{4}$$

To avoid finite-difference derivatives, it is common to fix the integer part of the occupation numbers and use $\{n_\alpha\}$ to denote the set of all ω_α's, $n_{p_\alpha}(\mathbf{r})$'s, and $n_{p_\alpha+1}(\mathbf{r})$'s. We also follow this convention in this text. Therefore, all our derivatives with respect to ω_α, $n_{p_\alpha}(\mathbf{r})$, or $n_{p_\alpha+1}(\mathbf{r})$ are not the "formal" derivatives but rather constrained derivatives

---

[⋆] Contribution to the Topical Issue "Special issue in honor of Hardy Gross", edited by C.A. Ullrich, F.M.S. Nogueira, A. Rubio, and M.A.L. Marques.

[a] e-mail: youeis@purdue.edu

that keep the integer part of the corresponding fragment α constant.

The inner minimization in equation (2) is done by the method of Lagrange multipliers. The equivalent unconstrained extremization is done for the following functional:

$$G[\{n_\alpha\}, v_{\rm p}(\mathbf{r})] = E_{\rm f}[\{n_\alpha\}] + \int d\mathbf{r} v_{\rm p}(\mathbf{r})[n_{\rm f}(\mathbf{r}) - n_{\rm GS}], \quad (5)$$

where the *partition potential*, $v_{\rm p}(\mathbf{r})$, has been introduced as the Lagrange multiplier that forces condition (4) to be satisfied at each point in space. Equation (5) also brings out the physical meaning of the fragment densities

$$n_\alpha(\mathbf{r}) = (1 - \omega_\alpha) n_{p_\alpha}(\mathbf{r}) + \omega_\alpha n_{p_\alpha+1}(\mathbf{r}). \quad (6)$$

They are the ensemble ground state densities of N_α electrons in the potential $(v_\alpha(\mathbf{r}) + v_{\rm p}(\mathbf{r}))$. The partition potential $v_{\rm p}(\mathbf{r})$ is the above-mentioned global embedding potential that guarantees the uniqueness of the n_α's [7]. Note that $E_{v_\alpha}[n_{p_\alpha}]$ in equation (3) is *not* the correct ground state energy corresponding to $n_{p_\alpha}(\mathbf{r})$, but $E_{v_\alpha+v_{\rm p}}[n_{p_\alpha}]$ is.

Stationarity of $G[\{n_\alpha\}, v_{\rm p}(\mathbf{r})]$ with respect to ω_α implies: [7]

$$\mu_\alpha^{\rm PT} = \mu_\beta^{\rm PT}, \quad (7)$$

for any two fragments α and β, where the α-chemical potential of PT is defined as

$$\begin{aligned} \mu_\alpha^{\rm PT} = &\left(E_{v_\alpha}[n_{p_\alpha+1}] + \int d\mathbf{r} v_{\rm p}(\mathbf{r}) n_{p_\alpha+1}(\mathbf{r})\right) \\ &- \left(E_{v_\alpha}[n_{p_\alpha}] + \int d\mathbf{r} v_{\rm p}(\mathbf{r}) n_{p_\alpha}(\mathbf{r})\right). \end{aligned} \quad (8)$$

Following the standard Kohn–Sham (KS) decomposition of the energy, the partition energy of equation (2) can be written as:

$$\begin{aligned} E_{\rm p}[n_N] = &T_{\rm s}^{\rm nad}[\{n_\alpha\}] + E_{\rm ext}^{\rm nad}[\{n_\alpha\}] + E_{\rm H}^{\rm nad}[\{n_\alpha\}] \\ &+ E_{\rm XC}^{\rm nad}[\{n_\alpha\}], \end{aligned} \quad (9)$$

where $T_{\rm s}$ is the noninteracting kinetic energy, $E_{\rm ext}$ is the interaction energy of electrons with the external potential, $E_{\rm H}$ is the Hartree energy, and $E_{\rm XC}$ is the exchange-correlation energy. The superscript "nad" indicates that each of these functionals is a non-additive contribution defined (for an arbitrary functional Π) as: $\Pi^{\rm nad}[\{n_\alpha\}] = \Pi[n_N] - \sum_\alpha \{(1 - \omega_\alpha) \Pi_\alpha[n_{p_\alpha}] + \omega_\alpha \Pi_\alpha[n_{p_\alpha+1}]\}$.

The relationship between $E_{\rm p}[\{n_\alpha\}]$ and $v_{\rm p}(\mathbf{r})$ was derived by Nafziger and Wasserman [8]:

$$\begin{aligned} v_{\rm p}(\mathbf{r}) = \int d\mathbf{r} \sum_\alpha \Bigg\{ &\frac{\delta E_{\rm p}}{\delta n_{p_\alpha}(\mathbf{r}')} \frac{\delta n_{p_\alpha}(\mathbf{r}')}{\delta n_{\rm f}(\mathbf{r})} \\ &+ \frac{\delta E_{\rm p}}{\delta n_{p_\alpha+1}(\mathbf{r}')} \frac{\delta n_{p_\alpha+1}(\mathbf{r}')}{\delta n_{\rm f}(\mathbf{r})} \Bigg\}. \end{aligned} \quad (10)$$

Substituting (9) into (10) leads to a useful decomposition of $v_{\rm p}(\mathbf{r})$ into contributions from kinetic, external, Hartree, and exchange-correlation parts.

Used with approximate density functionals, PT has been shown to fix delocalization and static correlation errors in bond-stretching [9]. It has also been successfully applied to the construction of approximations to non-additive noninteracting kinetic energy functionals [10,11]. The exact properties of PT were analyzed with numerically solvable model systems of noninteracting electrons [12–16] but the case of interacting electrons has only been studied approximately.

Here, for the first time, we solve the exact PT problem for systems of interacting electrons. We use simple 1-D models of hydrogen dimer (H_2), helium hydride cation (HeH^+) and lithium hydride (LiH) molecules. In these model cases, two valence electrons interact via a soft-Coulomb potential [17–19]. These models can be solved numerically exactly. We use these exact results to study the connection between KS and PT formalisms and the effect of electron–electron interaction on the most prominent features of the partition potential and its components.

2 Model system and numerical methods

The properties of each fragment as well as the entire system are computed on a fine real grid. Density-to-potential inversion techniques are used to solve the PT problem (i.e. the problem of finding $v_{\rm p}(\mathbf{r})$ for a given density and choice of partitioning). A more detailed discussion of the numerical methods is presented below.

2.1 Model Hamiltonians

Our model of a 1-D dimer has two interacting valence electrons. The soft-Coulomb (SC) potential is used to model charge-charge interactions. The electronic Hamiltonian is:

$$\begin{aligned} \mathcal{H} = \sum_{i=1,2} \Bigg\{ &-\frac{1}{2} \nabla_{x_i}^2 - \frac{1}{\sqrt{1.0 + (x_i - R_{\rm H})^2}} \\ &- \frac{Z_{\rm X}}{\sqrt{1.0 + (x_i - R_{\rm X})^2}} \Bigg\} + \frac{\lambda}{\sqrt{1.0 + (x_1 - x_2)^2}}, \end{aligned} \quad (11)$$

where x_i is the coordinate of the ith electron, $R_{\rm X}$ is the position of the nucleus X (X stands for either H or He), $Z_{\rm X}$ is the nuclear charge and λ is the parameter that switches the electron–electron interaction on ($\lambda = 1$) or off ($\lambda = 0$). We use the softening parameter value of 1.0 and a simulation box of 25 a.u. The case of LiH is discussed separately in equation (21).

With the nuclear-nuclear interaction given by:

$$V_{\rm nn} = \frac{Z_{\rm X}}{\sqrt{3.0 + (R_{\rm X} - R_{\rm H})^2}}, \quad (12)$$

the equilibrium bond-length is $R_0 = 1.6$ a.u. for H_2 and $R_0 = 2.1$ a.u. for HeH^+.

The fragment Hamiltonians have the form:

$$\mathcal{H}_{p_\alpha+1} = \sum_{i=1,2}\left\{-\frac{1}{2}\nabla_{x_i}^2 - \frac{Z_X}{\sqrt{1.0+(x_i-R_X)^2}} + v_p(x_i)\right\}$$
$$+ \frac{\lambda}{\sqrt{1.0+(x_1-x_2)^2}} \tag{13}$$

and

$$\mathcal{H}_{p_\alpha} = -\frac{1}{2}\nabla_x^2 - \frac{Z_X}{\sqrt{1.0+(x-R_X)^2}} + v_p(x). \tag{14}$$

2.2 Decomposition of $v_p(x)$

With the strategy introduced by equations (9) and (10), we rewrite $v_p(x)$ as:

$$v_p(x) = v_{p,\text{kin}}(x) + v_{p,\text{ext}}(x) + v_{p,\text{H}}(x) + v_{p,\text{XC}}(x), \tag{15}$$

where the components correspond to those of E_p in equation (9). To calculate each component, we note:

$$\frac{\delta T_s^{\text{nad}}[n_{p_\alpha}]}{\delta n_{p_\alpha}(x)} = (1-\omega_\alpha)(v_s[n_{p_\alpha}](x) - v_s[n_{\text{GS}}](x)), \tag{16a}$$

$$\frac{\delta E_\alpha^{\text{nad}}[n_{p_\alpha}]}{\delta n_{p_\alpha}(x)} = (1-\omega_\alpha)(v(x) - v_\alpha(x)), \tag{16b}$$

$$\frac{\delta E_H^{\text{nad}}[n_{p_\alpha}]}{\delta n_{p_\alpha}(x)} = (1-\omega_\alpha)\int dx_1\frac{n_{\text{GS}}(x_1)-n_{p_\alpha}(x_1)}{\sqrt{1.0+(x_1-x)^2}}, \tag{16c}$$

$$\frac{\delta E_{\text{XC}}^{\text{nad}}[n_{p_\alpha}]}{\delta n_{p_\alpha}(x)} = (1-\omega_\alpha)(v_{\text{XC}}[n_{\text{GS}}](x) - v_{\text{XC}}[n_{p_\alpha}](x)). \tag{16d}$$

The equivalent derivatives with respect to the $n_{p_\alpha+1}$ are omitted for brevity. The functional derivatives in equations (16) can be readily calculated and used further to obtain $v_{p,\text{kin}}(x)$, $v_{p,\text{ext}}(x)$ and $v_{p,\text{H}}(x)$. The remaining $v_{p,\text{XC}}(x)$ is calculated as a difference between the full $v_p(x)$ and the first three components. For the functional derivative $\delta n_{p_\alpha}(x')/\delta n_f(x)$ in equation (10), we use the local approximation [20]:

$$\frac{\delta n_{p_\alpha}(x')}{\delta n_f(x)} \approx \mathcal{Q}_{p_\alpha}(x,x') \equiv \frac{n_{p_\alpha}(x')}{n_f(x)}\delta(x-x'), \tag{17}$$

resulting in the following equations for the components:

$$v_{p,\text{kin}}(x) = \sum_\alpha\{\omega_\alpha\mathcal{Q}_{p_\alpha+1}(x,x)v_s^{(-)}[n_{p_\alpha+1}](x)$$
$$+(1-\omega_\alpha)\mathcal{Q}_{p_\alpha}(x,x)v_s^{(-)}[n_{p_\alpha}](x)\}$$
$$-v_s^{(-)}[n_{\text{GS}}](x), \tag{18a}$$

$$v_{p,\text{ext}}(x) = \sum_\alpha\left\{(v(x)-v_\alpha(x))\frac{n_\alpha(x)}{n_{\text{GS}}(x)}\right\}, \tag{18b}$$

$$v_{p,\text{H}}(x) = \sum_\alpha\left\{\omega_\alpha\mathcal{Q}_{p_\alpha+1}(x,x)\int dx_1\frac{n_{\text{GS}}(x_1)-n_{p_\alpha+1}(x_1)}{\sqrt{1.0+(x_1-x)^2}}\right.$$
$$\left.+(1-\omega_\alpha)\mathcal{Q}_{p_\alpha}(x,x)\int dx_1\frac{n_{\text{GS}}(x_1)-n_{p_\alpha}(x_1)}{\sqrt{1.0+(x_1-x)^2}}\right\}, \tag{18c}$$

$$v_{p,\text{XC}}(x) = v_{\text{XC}}^{(-)}[n_{\text{GS}}](x) - \sum_\alpha\{\omega_\alpha\mathcal{Q}_{p_\alpha+1}(x,x)v_{\text{XC}}^{(-)}[n_{p_\alpha+1}](x)$$
$$+(1-\omega_\alpha)\mathcal{Q}_{p_\alpha}(x,x)v_{\text{XC}}^{(-)}[n_{p_\alpha}](x)\}, \tag{18d}$$

where the superscript "$(-)$" indicates that the x-independent constant in $v_s(x)$ at integer electron number is calculated at the limit from below. Since this approximation satisfies the sum rule, $\sum_\alpha\{(1-\omega_\alpha)\mathcal{Q}_{p_\alpha} + \omega_\alpha\mathcal{Q}_{p_\alpha+1}\} = \delta(x-x')$ the sum of $v_p(x)$ components yields the *exact* $v_p(x)$ [20]. Although this local approximation was shown to be reliable for various systems [8], it can still affect the individual components. Finally, we note that since $v_s^{(-)}[n_{p_\alpha}](x) = v_\alpha(x) + v_H[n_{p_\alpha}](x) + v_{\text{XC}}^{(-)}[n_{p_\alpha}](x) + v_p(x)$, equations (18d) can be derived simply by construction.

2.3 Numerical methods

2.3.1 Exact diagonalization

Hamiltonians (11), (13) and (14) are all diagonalized on a real grid using the sixth order central finite difference method for the $\nabla_{x_i}^2$ operator [21]. We note that both (11) and (13) are symmetric under the particle index interchange and all the eigenstates are either symmetric or antisymmetric. Spatially symmetric solutions correspond to the spin zero state while the antisymmetric spatial solutions correspond to triplet spin states. It therefore becomes clear that we simply need to search for the lowest eigenstate of (13) or (14) [22,23].

2.3.2 Density-to-potential inversions

To obtain the exact $v_p(x)$, we need to perform a numerical inversion. The following outlines the inversion algorithm employed to find $v_p(x)$ for a particular partitioning at a fixed set of fragment occupation numbers:

0. Start with an initial guess for $v_p(x)$.
1. Use equations (4), (13) and (14) to compute the sum of fragment densities in the presence of $v_p(x)$.
2. Calculate the difference between the total molecular density and the sum from 1.
3. Based on the value from 2, decide whether the sum of the fragment densities is sufficiently close to the total molecular density. If it is, the optimization is done; otherwise go to 4.
4. Update $v_p(x)$. Go to step 1.

We note that the algorithm assumes that the total molecular density can be pre-computed. For the convergence criterion in step 3 we use the value of the following functional at step k:

$$\theta^{(k)}[n_f^{(k)}] = \frac{1}{2^2}\int dx[n_f^{(k)}(x) - n_{\text{GS}}(x)]^2, \tag{19}$$

where the factor 2 in the denominator appears because we have two electrons. For the update in step 4, we utilize the Broyden's method [24]. After the algorithm is converged, we methodically vary the occupation numbers to eventually scan the entire set and find the minimum. The initial guess of $v_{\mathrm{p}}(x) = 0$ in step 0 and the convergence thresholds of 10^{-14} in step 3 are sufficient for obtaining accurate energies. To obtain accurate and smooth potentials, we apply the following procedure. After the initial optimization to $\theta^{(k)} \sim 10^{-14}$, we compute $v_{\mathrm{p,kin}}^{(k)}(x)$, $v_{\mathrm{p,ext}}^{(k)}(x)$, $v_{\mathrm{p,H}}^{(k)}(x)$ and $v_{\mathrm{p,XC}}^{(k)}(x)$ using equation (18d). In particular, we use the exact molecular density to compute derivatives of equation (16) and the current $n_{\mathrm{f}}^{(k)}(x)$ to compute the factors of equation (17). We then use the computed potetials to find $\bar{v}_{\mathrm{p,kin}}(x) = v_{\mathrm{p}}^{(k)}(x) - v_{\mathrm{p,ext}}^{(k)}(x) - v_{\mathrm{p,H}}^{(k)}(x) - v_{\mathrm{p,XC}}^{(k)}(x)$ and $\bar{v}_{\mathrm{p,XC}}(x) = v_{\mathrm{p}}^{(k)}(x) - v_{\mathrm{p,ext}}^{(k)}(x) - v_{\mathrm{p,H}}^{(k)}(x) - v_{\mathrm{p,kin}}^{(k)}(x)$. Finally, we construct the new guess for $v_{\mathrm{p}}(x)$ by adding $\bar{v}_{\mathrm{p,kin}}(x)$, $\bar{v}_{\mathrm{p,XC}}(x)$, $v_{\mathrm{p,ext}}^{(k)}(x)$ and $v_{\mathrm{p,H}}^{(k)}(x)$. This new guess is run through a single cycle of the algorithm to return the improved results. This procedure does not significantly improve the energy results. However, it markedly improves the density convergence in the low-density regions and produces smooth potentials. Applying this procedure periodically within our algorithm can converge it to machine precision $(\max|n_{\mathrm{f}}^{(k)}(x) - n_{\mathrm{GS}}(x)| \sim 10^{-16})$. However, no appreciable changes in features of the potentials are observed after the threshold of $\theta \sim 10^{-14}$.

Since each fragment can only have up to 2 electrons, the KS potentials can be obtained analytically. The expressions for the inversions are trivial [25].

3 Illustrative results and discussion

3.3.1 H_2 model

We consider first a symmetric dimer model of H_2 at two different internuclear separations: the equilibrium bond length, $R_0 = 1.60$ a.u., and the large separation, $R = 10.0$ a.u. The optimal occupations for this model is clearly $N_{\mathrm{H,left}} = 1.0$ and $N_{\mathrm{H,right}} = 1.0$. We analyze features of $v_{\mathrm{p}}(x)$ and how they are affected by the electron–electron interaction. Our results highlight the importance of approximating $v_{\mathrm{p,kin}}(x)$ and $v_{\mathrm{p,XC}}(x)$ accurately in density embedding calculations, as previously pointed out by several computational studies using approximate $T_{\mathrm{s}}^{\mathrm{nad}}[n_{p_\alpha}]$ [10,11,26,27]. For the noninteracting system, we show that $v_{\mathrm{p}}(x)$ is dominated by $v_{\mathrm{p,ext}}(x)$ at equilibrium $(R_0 = 1.60)$ and by $v_{\mathrm{p,kin}}(x)$ $R_0 = 10.0$.

In Figure 1, we plot the PT deformations of the fragment densities $(\delta n_\alpha(x) = n_\alpha(x) - n_\alpha^0(x)$, where $n_\alpha^0(x)$ is the density of an isolated fragment) and partition potentials corresponding to these two cases. At $R = 10.0$, both densities are slightly shifted away from the interatomic region. In contrast, at the equilibrium separation, the densities are shifted towards the bonding region. Furthermore, the interatomic interactions are markedly weaker at the larger separation. This is reflected in

the density deformations and $v_{\mathrm{p}}(x)$ features that are roughly two orders of magnitude smaller than those at the equilibrium bond distance.

In the bottom panels of Figure 1, we analyze the origin of these features through the decomposition of equation (15). We combine $v_{\mathrm{p,ext}}(x)$ and $v_{\mathrm{p,H}}(x)$ because $v_{\mathrm{p,ext}}(x)$ has a deep well and $v_{\mathrm{p,H}}(x)$ has a high peak in the internuclear region. However, their sum is on the order of the features in $v_{\mathrm{p}}(x)$. Adding the external and Hartree components can be further justified by the fact that in practical calculations both can be computed exactly, but $v_{\mathrm{p,kin}}(x)$ and $v_{\mathrm{p,XC}}(x)$ require approximations. In the plot for $R = 10.0$, we also combine $v_{\mathrm{p,kin}}(x)$ and $v_{\mathrm{p,XC}}(x)$, as they are analyzed separately later in the paper. At the equilibrium, the depth of the well in $v_{\mathrm{p}}(x)$ is determined by the $v_{\mathrm{p,kin}}(x)$ and the $v_{\mathrm{p,ext}}(x) + v_{\mathrm{p,H}}(x)$ terms. The position of the peaks is also determined by the $v_{\mathrm{p,ext}}(x) + v_{\mathrm{p,H}}(x)$ contribution. We note that the effect of the non-additive XC term is small relative to the other components. At $R = 10.0$, the peak in the middle comes from $v_{\mathrm{p,ext}}(x) + v_{\mathrm{p,H}}(x)$. The contribution from $v_{\mathrm{p,kin}}(x)$ is almost completely cancelled by $v_{\mathrm{p,XC}}(x)$, but fine features persist even when the threshold $\theta^{(k)}$ is decreased to 10^{-23}.

It may appear that the contributions from $v_{\mathrm{p,kin}}(x)$ and $v_{\mathrm{p,XC}}(x)$ at large separation are unimportant as they cancel each other. However, the bottom right panel in Figure 2 shows that these features have high magnitude. Since in practice $v_{\mathrm{p,kin}}(x)$ and $v_{\mathrm{p,XC}}(x)$ are approximated separately, the accuracy of the total $v_{\mathrm{p}}(x)$ can be highly sensitive to the errors in these approximations.

In addition, Figure 2 shows the formation of $v_{\mathrm{p,kin}}(x)$ according to equation (18a). Top left panel shows $v_{\mathrm{s}}^{(-)}[n_{\mathrm{GS}}](x)$ along with $v_{\mathrm{s}}^{(-)}[n_{\mathrm{H}}](x)$'s. We observe that $v_{\mathrm{s}}^{(-)}[n_{\mathrm{H}}](x)$ matches closely with $v_{\mathrm{s}}^{(-)}[n_{\mathrm{GS}}](x)$ in the nuclear regions. The difference between the fragment and molecular KS potentials $\delta v_{\mathrm{s}}(x)$, plotted at the top right, has the flat region around their nucleus. The differences are weighted by the corresponding $n_{p_\alpha}(x)/n_{\mathrm{GS}}(x)$ terms and summed, producing the total $v_{\mathrm{p,kin}}(x)$. We note that $v_{\mathrm{p,kin}}(x)$ has a well from the peak in $v_{\mathrm{s}}^{(-)}[n_{\mathrm{GS}}](x)$. The peak in $v_{\mathrm{p,XC}}(x)$ has the *same* origin [28–31] and it nearly cancels the well in $v_{\mathrm{p,kin}}(x)$. This cancelation is not exact and the fine features in $v_{\mathrm{p,kin}}(x) + v_{\mathrm{p,XC}}(x)$ can still be observed.

We turn off the electron–electron interaction in the system by setting $\lambda = 0$. The results are shown in Figure 3. Our method recovers the trivial result that $v_{\mathrm{p,H}}(x)$ and $v_{\mathrm{p,XC}}(x)$ are zero. At both separations, $v_{\mathrm{p}}(x)$ has a single well. At equilibrium, this well is dominated by $v_{\mathrm{p,ext}}(x)$. In contrast, at $R = 10.0$, the well is predominantly determined by $v_{\mathrm{p,kin}}(x)$. The $v_{\mathrm{p}}(x)$ plots are consistent with previously reported ones for noninteracting systems [13,16], but the present work shows that the well in $v_{\mathrm{p}}(x)$ is dominated by different components at *different* internuclear distances.

3.3.2 HeH^+ model

We study the features of $v_{\mathrm{p}}(x)$ in the simplest heteronuclear molecular ion HeH^+ at equilibrium separation.
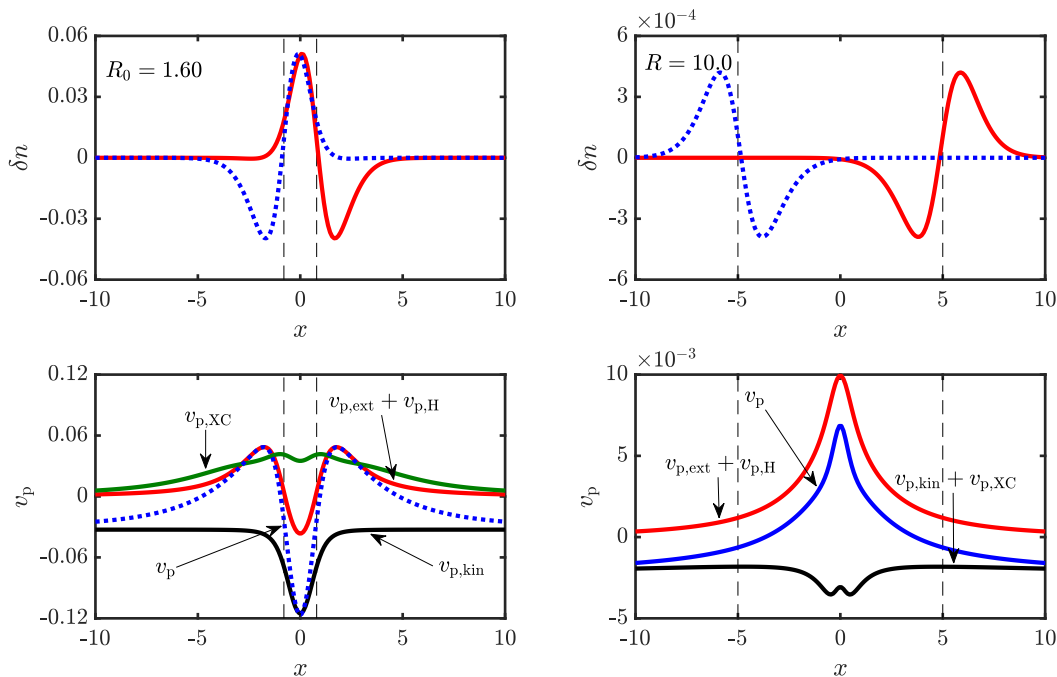
Fig. 1. 1-D H_2 model at $R_0 = 1.60$ a.u. (left) and $R = 10.0$ a.u. (right). Top: deformations of the fragment densities $\delta n_\alpha(x) = n_\alpha(x) - n_\alpha^0(x)$, where $n_\alpha^0(x)$ is the density of an isolated fragment. Bottom: partition potential $v_p(x)$ and its components defined through equation (15). Vertical dashed lines indicate the position of nuclei. The electron–electron interaction parameter $\lambda = 1$.
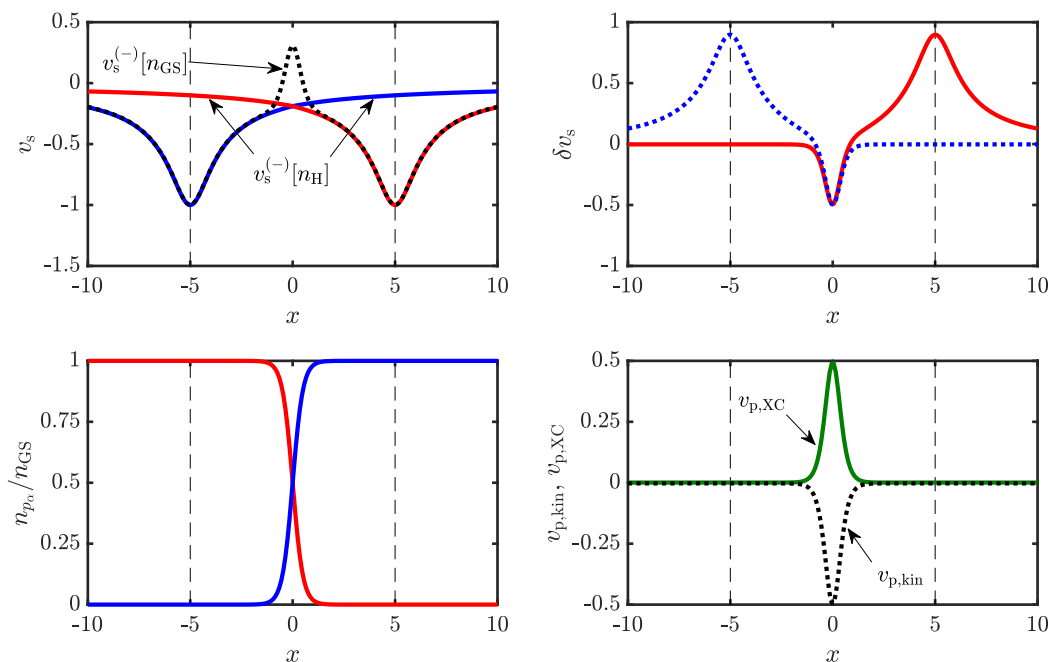
Fig. 2. The relationship between features of $v_{p,\text{kin}}(x)$ and the peak of molecular $v_s(x)$ for H_2 model at $\lambda = 1$ and $R = 10.0$. Top left: molecular KS potential $v_s^{(-)}[n_{\text{GS}}](x)$ and fragment KS potentials $v_s^{(-)}[n_H](x)$. Top right: the differences between the molecular and fragment potentials. Bottom left: $n_{p_\alpha}(x)/n_{\text{GS}}(x)$ terms. Bottom right: kinetic and XC contributions to the partition potential. Vertical dashed lines indicate the position of nuclei.
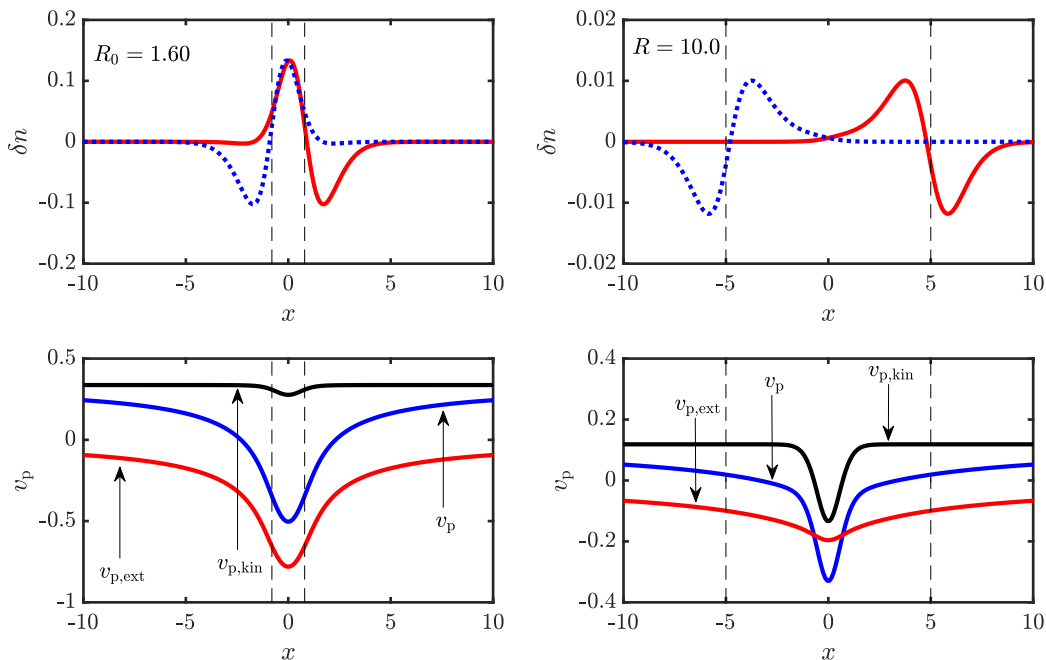
Fig. 3. Same as Figure 1, but for $\lambda = 0$.
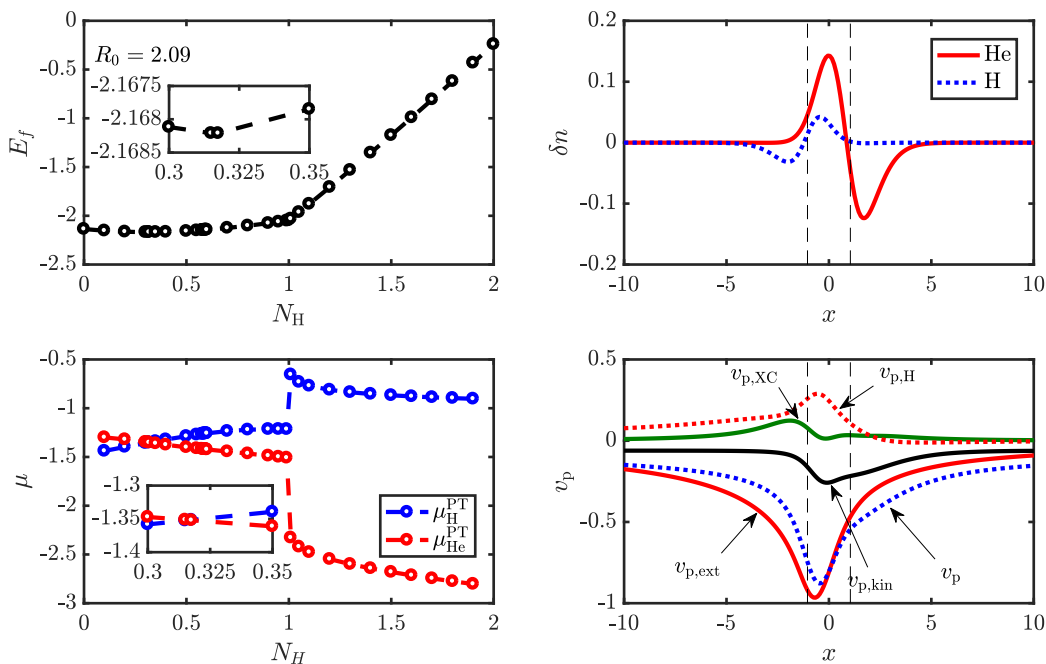
Fig. 4. Summary of the PT results for the model system of HeH$^+$ at equilibrium separation and $\lambda = 1$. Left: fragment energies (top) and PT chemical potentials (bottom) at varying occupations on H atom. Right: density deformations relative relative to the isolated fragments with the optimal electron occupations (top) and corresponding partition potential along its components (bottom). Vertical dashed lines indicate the position of nuclei (H is on the left).

This model has non-integer optimal occupations. We use this fact to analyze the relationship between the kinetic component of $v_\text{p}(x)$ and the KS gap of PT fragments.

The left two panels of Figure 4 show the behavior of $E_\text{f}[\{n_\alpha\}]$ as a function of the number of electrons on the hydrogen atom, at the equilibrium bond distance

of 2.09 $a.u.$ The curvature of the energy plot is an important consequence of accounting for the finite-distance interfragment interactions (in contrast, the plot of energy versus the number of electrons in DFT consists of straight-line segments). This curvature does not smoothen the graph at integer occupations, where it still
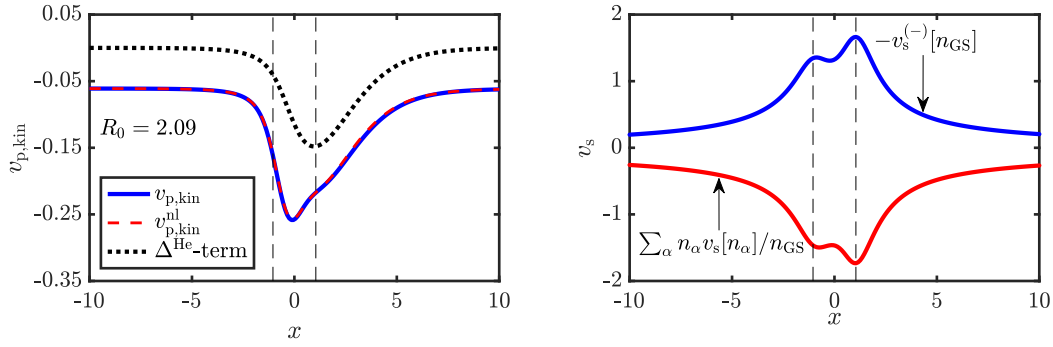
Fig. 5. The relationship between $v_{\mathrm{p,kin}}$ and Δ^{He} defined through equation (20). Δ^{He}-term stands for $-(1-\omega_{\mathrm{He}})\Delta^{\mathrm{He}}\mathcal{Q}_{p_{\mathrm{He}}}(x,x)$. Vertical dashed lines indicate the position of nuclei (H is on the left).

has a cusp. The graph has a minimum when $N_{\mathrm{H}} \approx 0.3175$. At this occupation, we also observe the chemical potential equalization of the fragments. A rigorous definition of fragments allows the discussion of the nature of a chemical bond and the optimal occupations suggest the amount of the ionic character a bond has. The connection between 1-D models and real bonds is, of course, not obvious. More generally, the physical interpretation of PT fragment properties is still an open question.

The top right panel of Figure 4 shows the density deformations relative to the isolated fragments with the optimal electron occupations. We observe that both He and H densities are shifted towards the interatomic region. The partition potential that facilitates this shift is plotted at the bottom right of Figure 4, along with its components. Although its overall shape is similar to H_2 at equilibrium bond distance, $v_{\mathrm{p}}(x)$ of HeH^+ is dominated by $v_{\mathrm{p,ext}}(x)$. Naively, this can be attributed to the fact that HeH^+ is an ion and the electron-nuclear interactions are the dominant ones.

The non-integer occupation numbers allow to establish the relationship between $v_{\mathrm{p,kin}}(x)$ and the fragment gaps $\Delta^\alpha = I^\alpha - A^\alpha$, where I^α is the ionization potential and A^α is the electron affinity of a fragment in the presence of $v_{\mathrm{p}}(x)$. If we assume the near-linearity of the fragment KS potentials [32], equation (18a) can be approximated as $v_{\mathrm{p,kin}}(x) \approx v_{\mathrm{p,kin}}^{\mathrm{nl}}(x)$, where:

$$
v_{\mathrm{p,kin}}^{\mathrm{nl}}(x) = \sum_\alpha \left\{ \frac{n_\alpha(x)}{n_{\mathrm{GS}}(x)} v_{\mathrm{s}}[n_\alpha](x) \right.
$$
$$
\left. - (1-\omega_\alpha)\Delta^\alpha \mathcal{Q}_{p_\alpha}(x,x) \right\} - v_{\mathrm{s}}^{(-)}[n_{\mathrm{GS}}](x).
$$
(20)

Figure 5 indicates that this approximation is in excellent agreement with the exact $v_{\mathrm{p,kin}}(x)$. The right panel in Figure 5 compares the molecular KS potential to the weighted sum of the fragment KS potentials, $\sum_\alpha n_\alpha[n_\alpha](x)/n_{\mathrm{GS}}(x)v_{\mathrm{s}}(x)$ from equation (20). We can see that these two contributions almost entirely cancel out and $v_{\mathrm{p,kin}}(x)$ is largely determined by the $(1-\omega_{\mathrm{He}})\Delta^{\mathrm{He}}\mathcal{Q}_{p_{\mathrm{He}}}(x,x)$ term (note that there is no contribution from Δ^{H} because $p_{\mathrm{H}} = 0$). Additional calculations on model systems suggest that the fragment KS term

closely mimics $-v_{\mathrm{s}}^{(-)}[n_{\mathrm{GS}}](x)$ in the high density regions, but it misses its low density peak-and-step features.

3.3.3 LiH model

We consider a heteroatomic dimer model of lithium hydride that separates into neutral fragments. In this model, the core electrons are not treated explicitly but their effects are simulated by adjusting the parameters of the external potential function. The modified electronic Hamiltonian of equation (11) is:

$$
\mathcal{H} = \sum_{i=1,2} \left\{ -\frac{1}{2}\nabla_{x_i}^2 - \frac{1}{\sqrt{2.25 + (x_i - R_{\mathrm{Li}})^2}} \right.
$$
$$
\left. - \frac{Z_{\mathrm{X}}}{\sqrt{0.6 + (x_i - R_{\mathrm{H}})^2}} \right\} + \frac{1}{\sqrt{0.7 + (x_1 - x_2)^2}},
$$
(21)

where the SC parameters for Li, H and electron–electron interactions (2.25, 0.70 and 0.60, respectively) are chosen following the same considerations as in reference [30]. These parameters produce the correct ionization potential difference between isolated Li and H atoms. The individual ionization potentials produced by this model are higher than the real ones, making the densities less diffuse and allowing us to use a simulation box of 25 a.u.

The results for LiH are summarized in Figure 6. The left two graphs show the fragment energies and chemical potentials at varying occupation numbers. E_{f} is minimized when N_{H} (and obviously N_{Li}) is equal to 1. This point is a cusp in E_{f} as expected from equation (3). $R = 10.0 \ a.u.$ can be taken as the large separation limit in our model and it shows that the bond breaking is homolytic. Although not obvious from the plot, the graph of E_{f} is curved, similar to the one for HeH^+ in Figure 4. The chemical potentials exhibit a step-like feature into integer occupations, which prevent the condition of equation (8) to be satisfied. The right two graphs show $v_{\mathrm{p}}(x)$ and its decomposition. Similarly to the case of H_2, $v_{\mathrm{p}}(x)$ has a peak in the internuclear region, dominated by the $v_{\mathrm{p,ext}}(x) + v_{\mathrm{p,H}}(x)$ term. Moreover, the $v_{\mathrm{p,kin}}(x)$ and $v_{\mathrm{p,XC}}(x)$ almost completely cancel out. Analogously to the case of H_2, their features are connected to the features of the molecular KS potential [28–31]. In addition to the peak, in this case, $v_{\mathrm{p,kin}}(x)$ and $v_{\mathrm{p,XC}}(x)$ also display a step. The steps
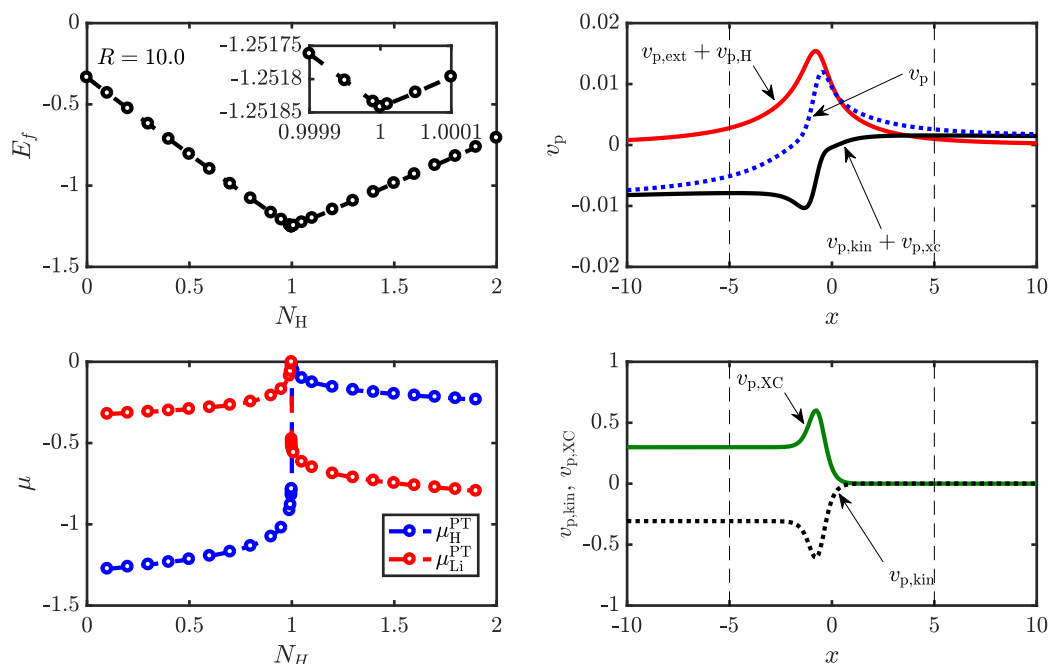
Fig. 6. Summary of the PT results for the model system of LiH, defined through equation (21) at $R = 10.0$. Left: fragment energies (top) and PT chemical potentials (bottom) at varying occupations on H atom. Right: partition potential and its components (top); kinetic and XC contributions to $v_p(x)$ (bottom). Vertical dashed lines indicate the position of nuclei (H is on the left).

almost entirely cancel out. The remaining small peak we observe in the top right panel of Figure 6 is likely due to the long range nature of SC potentials.

4 Concluding remarks

In spite of the simplicity of this model, we expect the same features discovered here to be present in real molecules. Explicit treatment of core electrons and 3D-Coulomb interactions would be of course needed to verify this.

Finally, the decomposition of $v_p(x)$ through equation (15) provides a useful way for identifying the origin of important features of $v_p(x)$ and linking them to the approximations used in practical density-embedding calculations. We plan to investigate in future work the extent to which approximate XC and non-additive kinetic energy functionals reproduce the features of $v_p(x)$ observed here.

Author contribution statement

Both authors contributed equally to this work.

References

1. R. Parr, W. Yang, *Density Functional Theory of Atoms and Molecules* (Oxford University Press, New York, 1989)
2. P.W. Ayers, R.G. Parr, J. Am. Chem. Soc. **129**, 2010 (2000)
3. P. Geerlings, F.D. Proft, W. Langenaeker, Chem. Rev. **103**, 1793 (2003)
4. M. Hellgren, E.K.U. Gross, J. Chem. Phys. **136**, 114102 (2012)
5. M.H. Cohen, A. Wasserman, J. Phys. Chem. A **111**, 2229 (2007)
6. J.P. Perdew, R.G. Parr, M. Levy, J.J.L. Balduz, Phys. Rev. Lett. **49**, 1691 (1982)
7. M.H. Cohen, A. Wasserman, J. Stat. Phys. **125**, 1121 (2006)
8. J. Nafziger, A. Wasserman, J. Phys. Chem. A **118**, 7623 (2014)
9. J. Nafziger, A. Wasserman, J. Chem. Phys. **143**, 234105 (2015)
10. J. Nafziger, K. Jiang, A. Wasserman, J. Chem. Theory Comput. **13**, 577 (2017)
11. K. Jiang, J. Nafziger, A. Wasserman, J. Chem. Phys. **148**, 104113 (2018)
12. M.H. Cohen, A. Wasserman, K. Burke, J. Phys. Chem. A **111**, 12447 (2007)
13. M. Cohen, A. Wasserman, R. Car, K. Burke, J. Phys. Chem. A **113**, 2183 (2009)
14. P. Elliott, M. Cohen, A. Wasserman, K. Burke, J. Chem. Theory Comput. **5**, 827 (2009)
15. P. Elliott, K. Burke, M. Cohen, A. Wasserman, Phys. Rev. A **82**, 024501 (2010)

16. R. Tang, J. Nafziger, A. Wasserman, Phys. Chem. Chem. Phys. **14**, 7780 (2012)
17. J.H. Eberly, Phys. Rev. A **42**, 5750 (1990)
18. M. Lein, E.K.U. Gross, V. Engel, J. Phys. B: At., Mol. Opt. Phys **33**, 433 (2000)
19. T.E. Baker, E.M. Stoudenmire, L.O. Wagner, K. Burke, S.R. White, Phys. Rev. B **91**, 235141 (2015)
20. M.A. Mosquera, A. Wasserman, Molecular Phys. **111**, 505 (2013)
21. B. Fornberg, Math. Comput. **51**, 699 (1988)
22. N. Helbig, J.I. Fuks, M. Casula, M.J. Verstraete, M.A.L. Marques, I.V. Tokatly, A. Rubio, Phys. Rev. A **83**, 032503 (2011)
23. S.A. Shpilkin, E.A. Smolenskii, N.S. Zefirov, J. Chem. Inf. Comput. Sci. **36**, 409 (1996)
24. C.G. Broyden, Math. Comput. **19**, 577 (1965)
25. D.S. Jensen, A. Wasserman, Int. J. Quantum Chem. **118**, e25425 (2018)
26. T.A. Wesołowski, A. Warshel, J. Phys. Chem. A **97**, 8050 (1993)
27. C.R. Jacob, J. Neugebauer, Wiley Interdiscip. Rev. Comput. Mol. Sci. **4**, 325 (2014)
28. O.V. Gritsenko, E.J. Baerends, Phys. Rev. A **54**, 1957 (1996)
29. N. Helbig, I.V. Tokatly, A. Rubio, J. Chem. Phys. **131**, 224105 (2009)
30. D.G. Tempel, T.J. Martínez, N.T. Maitra, J. Chem. Theory Comput. **5**, 770 (2009)
31. J.I. Fuks, S.E.B. Nielsen, M. Ruggenthalerbc, N.T. Maitra, Phys. Chem. Chem. Phys. **18**, 20976 (2016)
32. T. Gould, J. Toulouse, Phys. Rev. A **90**, 050502(R) (2014)